

## Chapter 2

# Theoretical Aspects of Photonic Structures

The fabrication of novel photonic devices is usually preceded by a design phase, involving the theoretical modelling of the device's optical behaviour, based on the properties of the applied materials. Various techniques have been developed for the theoretical study of light scattering, interference, or diffraction caused by photonic micro- and nano-structures [1–4]. Analytical treatments are only possible for some particular cases and many approaches have to rely on approximations or simulation of the electromagnetic fields in the structure of interest. Common approaches include:

- Transfer matrix techniques [2],
- Finite-difference time-domain (FDTD) and finite-difference frequency-domain (FDFD) simulations [3],
- Photonic band-gap calculations based on plane wave expansion [4].

These theoretical methods are very powerful tools, if one keeps aware of their limitations and interprets results correctly.

One of the main aspects of this thesis is the study of periodic multilayer structures, also called one-dimensional photonic crystals. Interference effects, occurring in flat multilayer structures can be treated analytically by using transfer matrix techniques [2] or by extending the derivation of the reflection coefficients of a single thin film to the case of any number of layers [5]. These calculations give precise solutions but cannot easily be extended to the treatment of non-planar structures.

The interaction of light with two- or three-dimensional photonic crystals can be investigated computationally with the freely available “MIT Photonic-Bands” package (MPB) [6] or the “MIT Electromagnetic Equation Propagation” software (MEEP) [7]. MPB computes definite-frequency eigenstates (harmonic modes) of Maxwell's equations in periodic dielectric structures for arbitrary wave-vectors in order to determine dispersion diagrams and electromagnetic modes in the dielectric medium. MEEP is a finite-difference time-domain (FDTD) simulation

package for the computation of transmission/reflection spectra, field patterns, resonant modes and frequencies in dielectric structures.

In this chapter the basics of reflection, refraction and interference in thin films are laid out and applied to the case of multilayer stacks made from lossless, linear dielectric materials. Several methods used for the characterisation of one-dimensional photonic crystals and simple diffraction elements are investigated and finally the suitability of MEEP for the modelling of diffraction from arbitrarily shaped periodic micro-structures is discussed.

## 2.1 Reflection and Refraction at Optical Interfaces

Assume a light wave impinging on an interface  $n_1|n_2$  between two, optically smooth dielectric materials with distinct refractive indices  $n_1$  and  $n_2$ , at an angle  $\theta_1$  with respect to the interface normal. Part of the wave is specularly reflected, while the rest is refracted (Fig. 2.1a). The reflected light leaves the interface obeying the condition  $\theta_r = -\theta_1$ , where  $\theta_r$  is the angle between the propagation direction of the reflected light and the interface normal. The refracted light propagates into the second medium at an angle  $\theta_2$  given by Snell's law

$$n_1 \cdot \sin \theta_1 = n_2 \cdot \sin \theta_2. \quad (2.1)$$

The electric field amplitudes  $E_r$  and  $E_t$  and intensities  $R$  and  $T$  of the reflected and the transmitted light depend on the polarisation of the incident light. Light that is polarized in the plane of incidence is referred to as parallel polarized light with

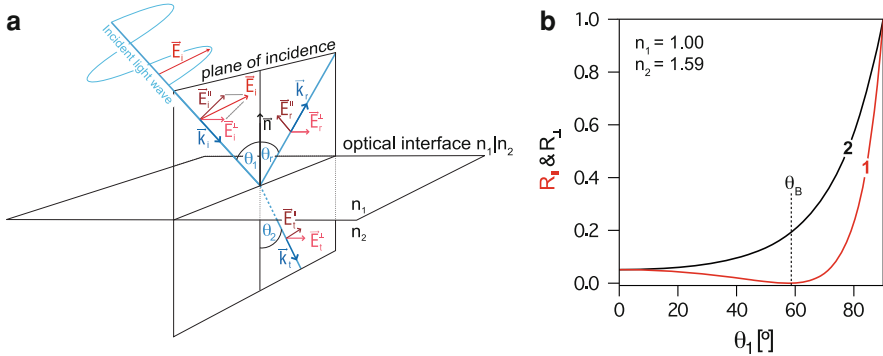


**Fig. 2.1** Reflection and refraction at an optical interface  $n_1|n_2$ . **a** The wave vectors of the incident, transmitted and reflected waves are  $\vec{k}_i$ ,  $\vec{k}_t$  and  $\vec{k}_r$ . The electric fields are  $\vec{E}_i$ ,  $\vec{E}_t$  and  $\vec{E}_r$ , decomposed into their components parallel and perpendicular to the plane of incidence,  $\vec{E}^{\parallel}$  and  $\vec{E}^{\perp}$ . **b** Reflectivity of an air | polystyrene interface for parallel (curve “1”, red in online version) and perpendicularly (curve “2”, black in online version) polarised light,  $R_{\parallel}$  and  $R_{\perp}$ , as a function of incidence angle  $\theta_1$ . At the Brewster angle  $\theta_B = 57.8^\circ$ ,  $R_{\parallel}$  vanishes and the reflected light is completely polarised perpendicularly to the plane of incidence

field amplitude  $E_{\parallel}$ . Light, that is polarized in the plane of the optical interface (normal to the plane of incidence) is termed perpendicularly polarized light with field amplitude  $E_{\perp}$ . Fresnel's reflection and transmission coefficients

$$\begin{aligned} r_{\parallel} &= \frac{E_{r,\parallel}}{E_{i,\parallel}} = \frac{n_2 \cos \theta_1 - n_1 \cos \theta_2}{n_2 \cos \theta_1 + n_1 \cos \theta_2} = \frac{\tan(\theta_1 - \theta_2)}{\tan(\theta_1 + \theta_2)} \\ r_{\perp} &= \frac{E_{r,\perp}}{E_{i,\perp}} = \frac{n_1 \cos \theta_1 - n_2 \cos \theta_2}{n_1 \cos \theta_1 + n_2 \cos \theta_2} = -\frac{\sin(\theta_1 - \theta_2)}{\sin(\theta_1 + \theta_2)} \\ t_{\parallel} &= \frac{E_{t,\parallel}}{E_{i,\parallel}} = \frac{2n_1 \cos \theta_1}{n_2 \cos \theta_1 + n_1 \cos \theta_2} \\ t_{\perp} &= \frac{E_{t,\perp}}{E_{i,\perp}} = \frac{2n_1 \cos \theta_1}{n_1 \cos \theta_1 + n_2 \cos \theta_2} \end{aligned} \quad (2.2)$$

provide a measure for the amplitudes of reflected and transmitted light.

The intensities of parallel- and perpendicularly-polarised, reflected and transmitted light  $R_{\parallel}, R_{\perp}$  and  $T_{\parallel}, T_{\perp}$  are then given by

$$\begin{aligned} R_{\parallel,\perp} &= r_{\parallel,\perp}^2 \\ T_{\parallel,\perp} &= \frac{n_2}{n_1} \cdot t_{\parallel,\perp}^2. \end{aligned} \quad (2.3)$$

For linearly polarized, incident light with a polarization angle  $\psi$  with respect to the plane of incidence the reflectivity is

$$R = R_{\parallel} \cdot \cos^2 \psi + R_{\perp} \cdot \sin^2 \psi. \quad (2.4)$$

It is worth noting, that  $R_{\perp}$  increases monotonously with increasing angle of incidence, while  $R_{\parallel} = 0$  at the Brewster angle (Fig. 2.1b). From the first line in Eq. 2.2, the Brewster angle,  $\theta_1 = \theta_B$ , is deduced from

$$\tan(\theta_2 + \theta_B) = 0,$$

that is (using Snell's law)

$$\theta_B = \arctan\left(\frac{n_2}{n_1}\right). \quad (2.5)$$

## 2.2 Thin Film Interference

The reflectivity of a thin, non absorbing layer of thickness  $d_1$  with refractive index  $n_1$ , bound by two semi-infinite media with refractive indices  $n_0$  and  $n_2$ , can be determined theoretically by summation over the amplitudes of all the light beams which leave the layer in reflection. Those beams might have incurred multiple

reflections within the layer (Fig 2.2). In the following, the Fresnel reflection and transmission coefficients of each of the two interfaces in the system are denoted  $r_{ij}$  or  $t_{ij}$ , with the index  $i$  denoting the medium from which a light beam hits an optical interface and index  $j$  representing the medium on the other side of that interface. The polarisation of the beam has to be taken into account in the determination of  $r_{ij}$  and  $t_{ij}$  but the subsequent treatment is identical for both polarisations, allowing us to drop the indices  $\perp$  and  $\parallel$ . From Fresnel's formulae it follows that  $r_{ij} = -r_{ji}$ . The length of the optical path travelled by a light ray in the thin layer dictates the shift in phase

$$\delta_m = (m + 1) \cdot \delta = (m + 1) \cdot \frac{2\pi}{\lambda} n_1 d_1 \cos \theta_1,$$

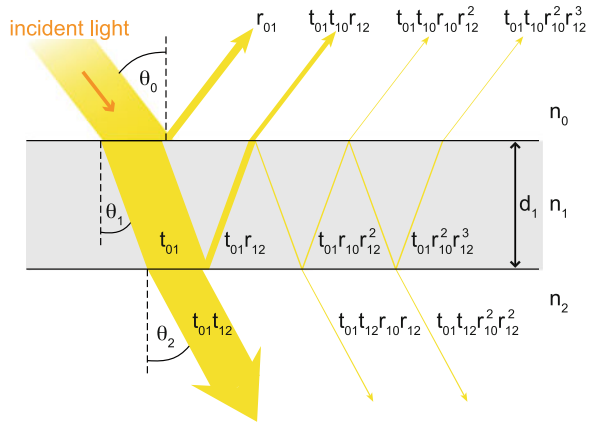
with  $\theta_1$  the angle of refraction in the layer and  $m$  the number of internal reflections. All the rays contributing to the overall reflectivity  $R$  of the film, have incurred an odd number of internal reflections (that is  $m + 1 = 2n$ , where  $n$  is a natural number). By summation over the amplitudes of these beams, taking into account their phase shift, the complex reflected amplitude  $A_r$  amounts to

$$\begin{aligned} A_r &= r_{01} + t_{01}t_{10}r_{12}e^{-2i\delta} \sum_{n=0}^{\infty} (-1)^n (r_{01}r_{12})^n e^{-2in\delta} \\ &= r_{01} + \frac{t_{01}t_{10}r_{12}e^{-2i\delta}}{1 + r_{01}r_{12}e^{-2i\delta}} \\ &= \frac{r_{01} + r_{12}e^{-2i\delta}}{1 + r_{01}r_{12}e^{-2i\delta}}. \end{aligned} \quad (2.6)$$

For the last equality in Eq. 2.6 the relation

$$t_{01}t_{10} = \sqrt{1 - r_{01}^2} \sqrt{1 - r_{10}^2} = 1 - r_{01}^2$$

**Fig. 2.2** Thin film reflectivity. Many of the light beams that are contributing to the overall reflectivity of the thin film have incurred multiple reflections in the layer, which determine their final amplitude when they leave the layer, based on Fresnel's reflection and transmission coefficients



has been used, essentially signifying the conservation of energy upon reflection and refraction.

Finally the reflectivity of a thin layer is given by

$$R = A_r A_r^* = \frac{r_{01}^2 + 2r_{01}r_{12} \cos 2\delta + r_{12}^2}{1 + 2r_{01}r_{12} \cos 2\delta + r_{01}^2 r_{12}^2}. \quad (2.7)$$

## 2.3 Multilayer Reflectivity

The reflectance behaviour of stacks of transparent, dielectric layers with distinct refractive indices results from the interference of light reflected from the different optical interfaces in the stack. This section focuses on multilayer stacks with  $N$  alternating layers of two different materials with refractive index  $n_1 > n_2$  and film thicknesses  $d_1, d_2$ . The stack is enclosed at the top and bottom by two (not necessarily different) media with refractive indices  $n_0$  and  $n_s$ . Coming from the upper medium, light impinges on the multilayer stack at an angle  $\theta_0$  (Fig. 2.3).

### 2.3.1 Qualitative Analysis of Multilayer Interference

Simple relations for the determination of the peak reflectance wavelength can be deduced by specifying the conditions for constructive interference of light beams that are reflected from the different optical interfaces in the stack (Fig. 2.3). Constructive interference of light, that is reflected off two consecutive interfaces

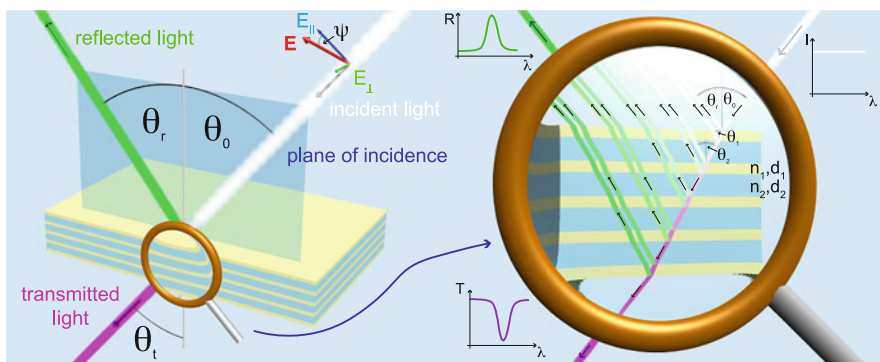


**Fig. 2.3** Multilayer interference. Reflection and transmission of light by a multilayer. Light beams reflected at the different interfaces in the multilayer stack interfere and cause the characteristic reflection and transmission spectra depending on the thickness and refractive index of the constituent materials

$n_1|n_2$ , is given, if the optical path length difference of the two light rays is equal to  $m \cdot \lambda$ , where  $m$  is a positive number. Purely geometrical considerations, taking into account Snell's law, lead to the relation

$$m \cdot \lambda = 2 \left( d_1 \cdot \sqrt{n_1^2 - n_0^2 \sin^2 \theta_0} + d_2 \cdot \sqrt{n_2^2 - n_0^2 \sin^2 \theta_0} \right), \quad (2.8)$$

which determines the wavelength  $\lambda$  at which constructive interference occurs.

For the interference of two rays that are reflected off two neighbouring interfaces  $n_1|n_2 - n_2|n_1$  (or  $n_2|n_1 - n_1|n_2$ ), an additional phase change of  $\pi$  has to be taken into account. This is justified by the fact that for all angles of incidence the Fresnel coefficients  $r_{\parallel}, r_{\perp}$  of the neighbouring interfaces are related by

$$r_{\parallel, \perp}^{n_1|n_2} = -r_{\parallel, \perp}^{n_2|n_1},$$

resulting in a additional contribution of  $\pi$  to the phase difference between two light beams reflected from the neighbouring interfaces. Consequently, constructive interference occurs, if the optical path difference is equal to  $(m' + \frac{1}{2}) \cdot \lambda$ , where  $m'$  is a positive number. This leads to

$$\left( m' + \frac{1}{2} \right) \cdot \lambda = 2d_j \cdot \sqrt{n_j^2 - n_0^2 \sin^2 \theta_0}, \quad (2.9)$$

where  $j$  stands for the respective layer.

Multilayer interference structures that satisfy Eqs. 2.8 and 2.9 are called “ideal” multilayers [8]. For non-ideal multilayer stacks the peak reflectance wavelength is determined by Eq. 2.8.

At normal incidence of light and  $m' = 0$ , Eq. 2.9 simplifies to  $\frac{\lambda}{4} = n_j d_j$ , hence the common name quarter-wave stack for ideal multilayer arrangements.

### 2.3.2 Quantitative Analysis of Multilayer Interference

#### 2.3.2.1 Rouard's Technique

The reflectivity of a multilayer structure can be calculated as a function of the relevant parameters wavelength of the incident light  $\lambda$ , refractive indices  $n_1, n_2$ , and film thicknesses  $d_1, d_2$  of the individual layers, layer number  $N$ , and angle of light incidence  $\theta_0$  using Rouard's technique [5]. Assuming the dielectric materials in the multilayer are transparent, the  $i$ th layer is fully characterised by its real-valued refractive index  $n_i$  and its layer thickness  $d_i$ . The bottom  $N - (i - 1)$  layers of the stack are referred to as the  $i$ th sub-stack. The  $i$ th layer in the entire multilayer is the first layer of the  $i$ th sub-stack. Consequently, the first sub-stack is the entire multilayer itself, while the  $(N + 1)$ th sub-stack is the bare substrate.

Starting at the substrate, the complex effective reflection coefficient  $\tilde{r}_i = \rho_i e^{iA_i}$  of the  $i$ th sub-stack is calculated by iteration. Insertion of the effective reflection coefficient  $\tilde{r}_{i+1}$  of the  $(i + 1)$ th sub-stack, that underlies the  $i$ th layer, in Eq. 2.6 gives

$$\tilde{r}_i = \rho_i e^{iA_i} = \frac{r_{i-1,i} + \rho_{i+1} e^{iA_{i+1}} e^{-2i\delta_i}}{1 + r_{i-1,i} \rho_{i+1} e^{iA_{i+1}} e^{-2i\delta_i}}, \quad (2.10)$$

where  $r_{i-1,i}$  is the reflection coefficient of the optical interface  $n_{i-1}|n_i$  between  $(i - 1)$ th and  $i$ th layer and  $\delta_i = \frac{2\pi}{\lambda} n_i d_i \cos \theta_0$  is the phase change that the light wave picks up as it traverses the  $i$ th layer.

### 2.3.2.2 Results

Rouard's technique was implemented in a MatLab algorithm. For user-friendliness, the program is equipped with a graphical user interface which allows for in situ variation of the multilayer parameters, such as refractive indices, film thicknesses, layer number, substrate and super-strate refractive indices or light incidence angle. Furthermore, a transfer matrix algorithm [2] has been compiled in a C++ routine to verify the data, acquired with the implementation of Rouard's method. Both programs produce matching results. Optical absorption in the individual layers or in the substrate material can be accounted for by working with complex refractive indices.

The reflectivity of a multilayer structure composed of two different materials with refractive indices  $n_1, n_2$  depends on the number of layers  $N$ , the refractive index contrast  $\hat{n} = \frac{n_1}{n_2}$  (assuming  $n_1 > n_2$ ), the polarisation of the incident light  $\psi$ , the thickness of the individual layers  $d_1, d_2$  and the angle of light incidence  $\theta_0$ . The influence of these parameters on the reflectivity of ideal multilayer quarter-wave stacks is investigated below. The reflectivity also depends on the underlying substrate and the super-strate but this dependence is not discussed in detail here.

With increasing number of layers  $N$  the reflectivity increases while the bandwidth of the reflection peak decreases (Fig. 2.4a). At light incidence angles  $\theta_0 \neq 0^\circ$ , the increase in reflectivity is more pronounced for perpendicularly-polarised light (Fig. 2.4b). For small enough layer numbers there is a significant difference between  $R_\perp$  and  $R_\parallel$  and consequently unpolarised light becomes partly polarized upon reflection from a multilayer. The difference between  $R_\parallel$  and  $R_\perp$  vanishes for a large number of layers in the stack.

Increasing the refractive index contrast  $\hat{n}$  leads to an increase in reflectivity (Fig. 2.4c). The increase is more pronounced for perpendicularly-polarised light but for high contrasts the difference between  $R_\perp$  and  $R_\parallel$  vanishes (Fig. 2.4d).

For increasing angles of light incidence  $R_\perp$  increases monotonically towards unity while  $R_\parallel$  first decreases, reaching a minimum at the generalised Brewster angle  $\theta_{gB}$  of the multilayer stack [9], before it increases again.

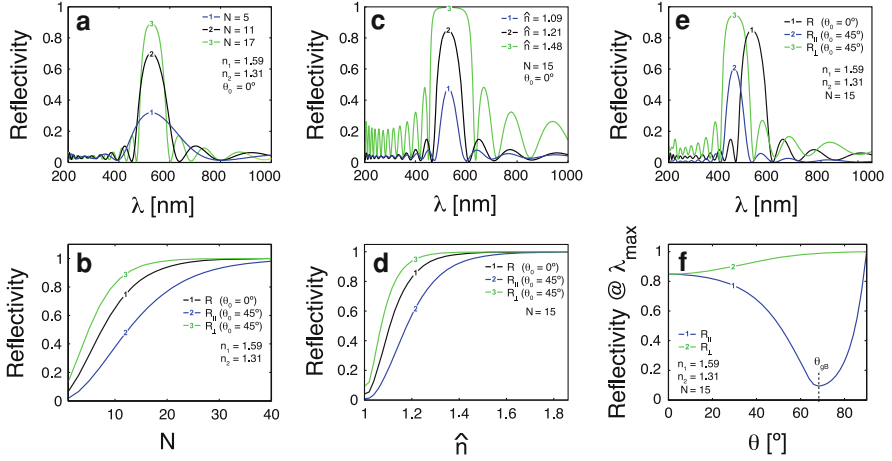


**Fig. 2.4** Multilayer reflectivity. **a** Reflectivity versus wavelength  $\lambda$  for different layer numbers  $N$  at normal light incidence  $\theta_0 = 0^\circ$ . **b** Reflectivity of parallel- and perpendicularly-polarised light versus layer number  $N$  for  $\theta_0 = 0^\circ$  and  $\theta_0 = 45^\circ$ . **c**  $R(\lambda)$  for different refractive index contrasts  $\hat{n} = \frac{n_1}{n_2}$  at constant layer number  $N = 15$  and  $\theta_0 = 0^\circ$ . **d**  $R_{\parallel}$  and  $R_{\perp}$  versus  $\hat{n}$  for  $\theta_0 = 0^\circ$  and  $\theta_0 = 45^\circ$ ,  $N = 15$ . **e**  $R_{\parallel}$  and  $R_{\perp}$  versus wavelength for  $\theta_0 = 0^\circ$  and  $\theta_0 = 45^\circ$ ,  $N = 15$ ,  $\hat{n} = 1.21$ . **f**  $R_{\parallel}(\lambda_{\max})$  and  $R_{\perp}(\lambda_{\max})$  versus  $\theta_0$ ,  $N = 15$ ,  $\hat{n} = 1.21$

The change in reflectance peak wavelength  $\lambda_{\max}$  is more pronounced if the refractive index of the optically thinner material is lower (Fig. 2.5a, b). For increasing layer number and increasing refractive index contrast, the variation in polarisation angle  $\psi$  that the light incurs upon reflection decreases (Fig. 2.5c, d), provided the incidence angle  $\theta_0$  is kept constant. The generalised Brewster angle  $\theta_{gB}$ , at which the reflectivity for parallel polarised light  $R_{\parallel}$  drops drastically, increases as the number of layers is increased (Fig. 2.5e, f). Provided the angle of incidence of unpolarised light matches  $\theta_{gB}(N)$  of the multilayer, high reflectivity can be achieved, while the reflected light is strongly polarised.

In general, a multilayer structure has to be tailored to its specific purpose by using appropriate materials and by suitably adapting the film thicknesses. Some guidelines based on the above presented discussions are given in Table 2.1.

## 2.4 Band-Gaps of One-Dimensional Photonic Crystals

A photonic crystal is a material with refractive index varying periodically (on a length scale comparable to the wavelengths of light) in one, two or all three spatial dimensions. Multilayer stacks are often called one-dimensional photonic crystal structures due to their periodicity perpendicular to the layer planes. The term “photonic crystal” was inspired by Eli Yablonovitch and Sajeev John in 1987,



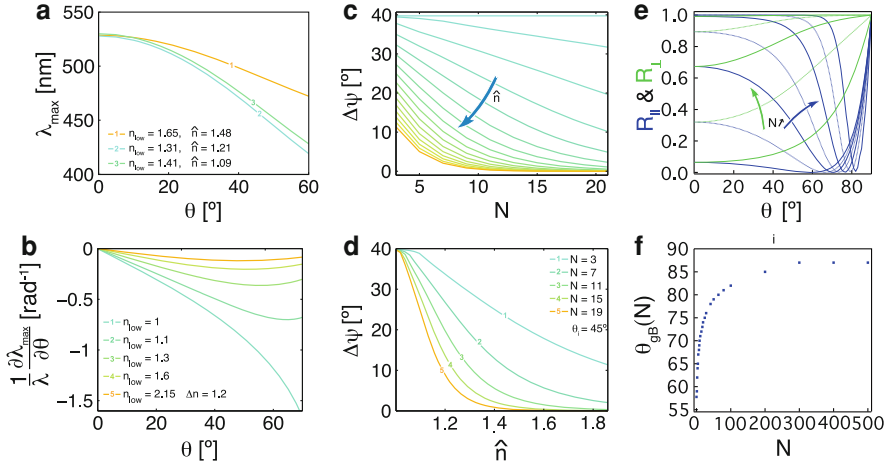


**Fig. 2.5** Peak wavelength and polarisation. **a** Peak wavelength  $\lambda_{\max}$  as a function of light incidence angle  $\theta_0$  for varying refractive indices  $n_{\text{low}}$  of the optically thinner material in the multilayer stack. **b** Variation of peak wavelength as a function  $\theta_0$  for different refractive indices  $n_{\text{low}}$ . **c** Rotation of light polarisation after reflection for  $\theta_0 = 45^\circ$  as a function of layer number  $N$  and refractive index contrast  $\hat{n}$ . Incident light is polarised by  $\psi = 45^\circ$ . **d** Polarisation variation for  $\theta_0 = 45^\circ, \psi = 45^\circ$  as a function of refractive index contrast  $\hat{n}$  for different layer numbers  $N$ . **e**  $R_{\parallel}$  (blue) and  $R_{\perp}$  (green) as a function of incidence angle  $\theta_0$  for increasing layer number. **f** Variation of the generalised Brewster angle  $\theta_{gB}(N)$  at which  $R_{\parallel}$  is minimal, as a function of layer number

**Table 2.1** Optical properties of multilayer stacks depending on their design where  $\Delta\lambda$  is the reflectance peak-width,  $\theta_0$  the light incidence angle,  $\Delta\psi$  the change in polarisation upon reflection,  $N$  the layer number,  $\hat{n}$  the refractive index contrast,  $n_{\text{low}}$  the lower refractive index in the multilayer and  $d_i$  the thickness of the individual layers with refractive index  $n_i$

| Desired optical properties |                 |  |              | Design requirements |           |                  |                               |                  |
|----------------------------|-----------------|--|--------------|---------------------|-----------|------------------|-------------------------------|------------------|
| Reflectivity               | $\Delta\lambda$ | $\frac{\partial\lambda}{\partial\theta_0}$ | $\Delta\psi$ | $N$                 | $\hat{n}$ | $n_{\text{low}}$ | $d_i$                         | $\theta_0$       |
| High                       | High            | —  | —            | Moderate ( $>10$ )  | High      | —                | $\frac{\lambda_{\max}}{4n_i}$ | —                |
| High                       | Low             | —  | —            | High                | Low       | —                | $\frac{\lambda_{\max}}{4n_i}$ | —                |
| High                       | Low             | High                                       | —            | High                | Low       | $\simeq 1$       | $\frac{\lambda_{\max}}{4n_i}$ | —                |
| High                       | High            | Low  | —            | High                | High      | High             | $\frac{\lambda_{\max}}{4n_i}$ | —                |
| $R_{\perp}$ high           | —               | —  | High         | Low                 | Low       | —                | $\frac{\lambda_{\max}}{4n_i}$ | $\theta_{gB}(N)$ |

“—” signifies “of minor relevance”

who joined the tools of classical electromagnetism and solid-state physics to introduce the concepts of omnidirectional photonic band gaps in two and three dimensions. Since then, not only the well-studied Bragg reflectors and filters with band-gaps in one dimension, but especially two- and three-dimensional photonic structures used for “molding the flow of light” [4] have received considerable

research interest. The band-gaps of a photonic structure are the frequency ranges for which light cannot propagate through this structure.

A common treatment of one-dimensional infinitely extended photonic crystals is based on a plane wave expansion technique. The discussion of this approach is focussed on photonic crystals consisting of lossless, linear dielectrics with no internal current sources and with magnetic permeability  $\mu_0 \approx 1$ . This does not include metals, or non-linear materials with optical absorption. Nevertheless, it provides excellent insight in the properties of photonic crystals and is appropriate for most of the optical structures found in nature. At the end of this section, the band diagrams of three different multilayer material systems, which are relevant to this thesis, are calculated.

The Maxwell equations that describe the link between a light wave's electric field  $\vec{E}(\vec{r}, t)$  and its magnetic field  $\vec{H}(\vec{r}, t)$  can be written in the following form

$$\begin{aligned} \nabla \cdot \vec{H}(\vec{r}, t) &= 0 & \nabla \times \vec{E}(\vec{r}, t) &= -\frac{1}{c} \frac{\partial \vec{H}(\vec{r}, t)}{\partial t} \\ \nabla \cdot \varepsilon(\vec{r}) \vec{E}(\vec{r}, t) &= 0 & \nabla \times \vec{H}(\vec{r}, t) &= \frac{\varepsilon(\vec{r})}{c} \frac{\partial \vec{E}(\vec{r}, t)}{\partial t}, \end{aligned} \quad (2.11)$$

where  $\varepsilon(\vec{r})$  is the periodically varying dielectric function of the photonic crystal and  $c$  is the speed of light.

Electric or magnetic fields can in principle be decomposed into time-harmonic Fourier modes. Consequently, we can limit this discussion to the treatment of time-harmonic field patterns

$$\begin{aligned} \vec{H}(\vec{r}, t) &= \vec{H}(\vec{r}) e^{i\omega t} \\ \vec{E}(\vec{r}, t) &= \vec{E}(\vec{r}) e^{i\omega t} \end{aligned}$$

for which Maxwell's equations are given by

$$\begin{aligned} \nabla \cdot \vec{H}(\vec{r}, t) &= 0 & \nabla \times \vec{E}(\vec{r}, t) &= -\frac{i\omega}{c} \vec{H}(\vec{r}, t) \\ \nabla \cdot \varepsilon(\vec{r}) \vec{E}(\vec{r}, t) &= 0 & \nabla \times \vec{H}(\vec{r}, t) &= \varepsilon(\vec{r}) \cdot \frac{i\omega}{c} \vec{E}(\vec{r}, t) \end{aligned} \quad (2.12)$$

From this equation system the wave equations for the magnetic and the electric field can be deduced.

$$\begin{aligned} \nabla \times \left( \frac{1}{\varepsilon(\vec{r})} \cdot \nabla \times \vec{H}(\vec{r}) \right) &= \left( \frac{\omega}{c} \right)^2 \vec{H}(\vec{r}) \\ \frac{1}{\varepsilon(\vec{r})} \cdot \nabla \times (\nabla \times \vec{E}(\vec{r})) &= \left( \frac{\omega}{c} \right)^2 \vec{E}(\vec{r}) \end{aligned} \quad (2.13)$$

These equations essentially represent two eigenvalue problems

$$\begin{aligned}\mathbf{O}_H \vec{H}(\vec{r}) &= \left(\frac{\omega}{c}\right)^2 \vec{H}(\vec{r}) \\ \mathbf{O}_E \vec{E}(\vec{r}) &= \left(\frac{\omega}{c}\right)^2 \vec{E}(\vec{r})\end{aligned}\tag{2.14}$$

with the operators

$$\begin{aligned}\mathbf{O}_H \vec{H}(\vec{r}) &= \nabla \times \left( \frac{1}{\varepsilon(\vec{r})} \cdot \nabla \times \vec{H}(\vec{r}) \right) \\ \mathbf{O}_E \vec{E}(\vec{r}) &= \frac{1}{\varepsilon(\vec{r})} \cdot \nabla \times (\nabla \times \vec{E}(\vec{r})).\end{aligned}$$

Both operators are linear and the operator  $\mathbf{O}_H$  is Hermitian, which is not necessarily the case for the operator  $\mathbf{O}_E$  [4]. The eigenvalues of Hermitian operators are real, and two eigenmodes  $\vec{H}_1(\vec{r}), \vec{H}_2(\vec{r})$  with eigenvalues  $\omega_1 \neq \omega_2$  are orthogonal to each other, that is the inner product vanishes:

$$(\vec{H}_1(\vec{r}), \vec{H}_2(\vec{r})) \equiv \int \vec{H}_1^*(\vec{r}) \cdot \vec{H}_2(\vec{r}) d\vec{r} = 0.$$

In addition, the eigenmodes of a Hermitian operator can be classified by their symmetry properties and valuable information can be obtained about the symmetry of field modes, arising from the symmetry in the dielectric function  $\varepsilon(\vec{r})$  of the material.

In the following, the eigenvalue problem is solved for infinitely extended stacks of alternating layers made from two optically distinct, lossless dielectric materials with refractive indices  $n_1, n_2$  and thicknesses  $d_1, d_2$ . This system has a high symmetry in one dimension and the direction of periodicity is chosen to be the  $z$ -coordinate of the associated reference system. Similar systems have already been investigated earlier in this chapter, using traditional approaches, such as the transfer matrix technique or Rouard's method. Here, the main focus is directed towards the analysis of the band structure of a layered system. This technique can be generalised to two- or three-dimensional photonic crystals. The dielectric function  $\varepsilon(\vec{r})$  of the infinite multilayer with layer thicknesses  $d_1, d_2$  and unit cell length  $p = d_1 + d_2$  is given by

$$\varepsilon(\vec{r}) = \varepsilon(z) = \begin{cases} n_1 : & mp - \frac{d_1}{2} \leq z < mp + \frac{d_1}{2} \\ n_2 : & (m + \frac{1}{2})p - \frac{d_2}{2} \leq z < (m + \frac{1}{2})p + \frac{d_2}{2} \end{cases}\tag{2.15}$$

where  $m$  is a positive number.

It can easily be shown that the operator  $\mathbf{O}_E$  is hermitian<sup>1</sup> for this particular dielectric function  $\varepsilon(\vec{r})$ . This allows us to draw conclusions about the symmetry of

---

<sup>1</sup> This is done by showing that the inner product  $(\vec{E}_1(\vec{r}), \mathbf{O}_E \vec{E}_2(\vec{r})) = (\mathbf{O}_E \vec{E}_1(\vec{r}), \vec{E}_2(\vec{r}))$  for any vector fields  $\vec{E}_1(\vec{r})$  and  $\vec{E}_2(\vec{r})$ .

the fields in the multilayer structure based on the symmetry of the system. The symmetry argument is outlined below, followed by the application of the plane wave expansion technique to find the electric field distributions  $\vec{E}(\vec{r})$  of the eigenmodes and the corresponding eigenfrequencies of  $\mathbf{O}_E$ . The corresponding magnetic field distributions  $\vec{H}(\vec{r})$  can then be deduced from  $\vec{E}(\vec{r})$  via Maxwell's equations.<sup>2</sup>

The multilayer system is translationally invariant for any displacement  $\vec{\rho} = x\hat{x} + y\hat{y}$  in the plane of the layers, where  $\hat{x}$  and  $\hat{y}$  are unit vectors along the  $x$ - and  $y$ -direction. That is  $\varepsilon(\vec{r} + \vec{\rho}) = \varepsilon(\vec{r})$ . The amplitude of the eigenmodes of a system with translational invariance in  $x$ - and  $y$ -direction can only be a function of the  $z$ -coordinate. The phase relationship between different points in the photonic crystal with the same  $z$ -coordinate is given by the wave vector component  $\vec{k}_\rho = k_x\hat{x} + k_y\hat{y}$ . Thus the eigenmodes have the form

$$\vec{E}_{k_\rho}(x, y, z) = e^{i\vec{k}_\rho \vec{\rho}(x, y)} \cdot \vec{e}(z) \quad (2.16)$$

where the field amplitude  $\vec{e}$  is only dependent on the spatial variable  $z$ .

Due to the discrete symmetry of the system in  $z$ -direction, the eigenmodes must be periodic along the  $z$ -coordinate, that is

$$\vec{E}(x, y, z + p) = e^{i\vec{k}_\rho \vec{\rho}(x, y)} \cdot \vec{e}(z + p) = e^{i\vec{k}_\rho \vec{\rho}(x, y)} \cdot \vec{e}(z) = \vec{E}(x, y, z),$$

where  $p$  is the period of the system. According to Bloch's theorem [10], the periodic wave function  $\vec{e}(z)$  can be expressed by a product of a plane wave with a  $z$ -periodic function

$$\vec{e}_{k_z}(z) = e^{ik_z z} \vec{u}_{k_z}(z) \quad (2.17)$$

and consequently the eigenmodes of such a periodic system, also known as Bloch states, are given in general by

$$\vec{E}_{\vec{k}}(\vec{r}) = e^{i\vec{k}\vec{r}} \cdot \vec{u}_{\vec{k}}(\vec{r}). \quad (2.18)$$

For light travelling along the  $z$ -direction this simplifies to the scalar relation

$$E_{k_z}(z) = e^{ik_z z} \cdot u_{k_z}(z). \quad (2.19)$$

Bloch states with wave-vectors  $k_z$  and  $k_z + m \cdot \frac{2\pi}{p}$  are identical from a physical point of view. Thus, the eigenvalues of these Bloch states, which represent the frequencies of the corresponding modes, must also be periodic in  $k_z$ , that is  $\omega(k_z) = \omega\left(k_z + m \cdot \frac{2\pi}{p}\right)$ . The Brillouin zone is the region in a dispersion diagram

---

<sup>2</sup> Working with the electric field rather than the magnetic field, is only justified by the fact, that the plane wave expansion technique is less cumbersome but the approach would be the same for the magnetic field.

$\omega(k)$  which contains only the non-redundant wave vectors  $k_z$  in the range  $-\frac{\pi}{p} < k_z \leq \frac{\pi}{p}$ . The band structure of a photonic crystal is known, if the dispersion relation  $\omega(k)$  in its Brillouin zone is determined. This can be done with a plane wave expansion technique.

Assuming for simplicity a wave with a field vector only along the  $x$ -direction,  $\vec{E}(\vec{r}) = E_x(\vec{r}) \cdot \hat{x}$ , the wave equation

$$\frac{1}{\varepsilon(\vec{r})} \cdot \nabla \times \nabla \times \vec{E}(\vec{r}) = \frac{\omega^2}{c^2} \vec{E}(\vec{r}) \quad (2.20)$$

simplifies to

$$\frac{1}{\varepsilon(\vec{r})} \left( -\frac{\partial^2 E_x(\vec{r})}{\partial y^2} - \frac{\partial^2 E_x(\vec{r})}{\partial z^2} \right) = \left( \frac{\omega}{c} \right)^2 E_x(\vec{r}), \quad (2.21)$$

where  $\varepsilon(\vec{r})$  is given by Eq. 2.15. Fourier-expansion of the field and the inverse dielectric function  $\frac{1}{\varepsilon}$  yields

$$\begin{aligned} E_x(z) &= \sum_{t=-\infty}^{\infty} \tilde{E}_t e^{-\frac{2\pi i t}{p} z} \\ \frac{1}{\varepsilon(z)} &= \sum_{s=-\infty}^{\infty} \tilde{\varphi}_s e^{-\frac{2\pi i s}{p} z}, \end{aligned} \quad (2.22)$$

where  $\tilde{E}_t$  and  $\tilde{\varphi}_s$  are the Fourier coefficients of the field  $E_x(z)$  and the admittance  $\frac{1}{\varepsilon(z)}$ , respectively. Inclusion of the Fourier expansions in the wave equation gives, after reorganisation and simplification, the eigenequation that has to be solved in order to determine the band diagram:

$$\sum_{t=-\infty}^{\infty} \left( \frac{2\pi t}{p} + k_z \right)^2 \tilde{\varphi}_{s-t} \tilde{E}_t = \left( \frac{\omega}{c} \right)^2 \tilde{E}_s. \quad (2.23)$$

After symmetric truncation ( $|t| \leq t_{\max}$ ,  $|s| \leq s_{\max}$ ) of the Fourier series of  $E_x(z)$  and  $\frac{1}{\varepsilon(z)}$ , this equation becomes an eigenvalue problem which can be written in the form

$$\mathbf{O}_{s,t} \tilde{E}_t = \left( \frac{\omega}{c} \right)^2 \tilde{E}_s \quad (2.24)$$

with  $\mathbf{O}_{s,t}$  being a  $2s_{\max} + 1$  by  $-2t_{\max} + 1$  matrix with its elements  $O_{s,t}$  given by

$$O_{s,t} = \left( \frac{2\pi t}{p} + k_z \right)^2 \tilde{\varphi}_{s-t}.$$

The Fourier coefficients  $\tilde{\varphi}_{s-t}$  can be found by using the inverse Fourier transform

$$\begin{aligned}
 \tilde{\varphi}_{s-t} &= \frac{1}{p} \int_{-\frac{p}{2}}^{\frac{p}{2}} \frac{1}{\varepsilon(z)} \cdot e^{\frac{2\pi i(s-t)}{p}z} dz \\
 &= \frac{1}{p} \left( \int_{-\frac{p}{2}}^{-\frac{d_1}{2}} \frac{1}{n_2^2} \cdot e^{\frac{2\pi i(s-t)}{p}z} dz + \int_{-\frac{d_1}{2}}^{\frac{d_1}{2}} \frac{1}{n_1^2} \cdot e^{\frac{2\pi i(s-t)}{p}z} dz + \int_{\frac{d_1}{2}}^{\frac{p}{2}} \frac{1}{n_2^2} \cdot e^{\frac{2\pi i(s-t)}{p}z} dz \right) \quad (2.25) \\
 &= \frac{1}{n_2^2} \cdot \delta_{s-t} + \left( \frac{1}{n_1^2} - \frac{1}{n_2^2} \right) \cdot \text{sinc} \left( \frac{\pi(s-t)d_1}{p} \right).
 \end{aligned}$$

By computational diagonalisation of the matrix  $\mathbf{O}_{s,t}$ , its eigenvectors  $\tilde{E}$  and the corresponding eigenvalues  $(\frac{\omega}{c})^2$  can be determined. The eigenvectors  $\tilde{E}$  can be introduced back into the Fourier expansion of  $\vec{E}$  to find the field distribution. The eigenvalues give the dispersion diagram.

Each infinite multilayer stack of two optically distinct dielectrics ( $n_1 \neq n_2$ ), has band-gaps. Their extent depends on the refractive index contrast of the constituent materials. Figure 2.6 shows the calculated band-gaps of multilayer stacks made from three different material combinations. The corresponding materials, their refractive indices and layer thicknesses are displayed in Table 2.2. Band-gaps are wider for larger refractive index contrasts. Figure 2.6d shows the field distributions of three modes lying at the edge of the Brillouin zone ( $k_z = \frac{\pi}{p}$ ) for a material combination with refractive index contrast  $\hat{n} = 1.21$ . The position of these modes on the three lowest bands are marked in Fig. 2.6b. For the minimisation of its energy, the electric field of the ground mode (1), tends to be located in the regions of high dielectric constant  $\varepsilon$ . The modes with higher frequencies than the ground mode tend to concentrate their field in the high dielectric material obeying the constraint of remaining orthogonal to the modes that have a lower frequency [4].

The band-diagrams shown in Fig. 2.6 correspond to multilayer stacks that have been fabricated from the material combinations, displayed in Table 2.2. These structures are presented in detail in Chap. 4.

## 2.5 Multilayer Resonance Cavities

One-dimensional multilayer resonance cavities, so called interference filters or Bragg filters, usually consist of a “defect” layer of  $m \cdot \frac{\lambda}{2}$ -thickness, introduced into

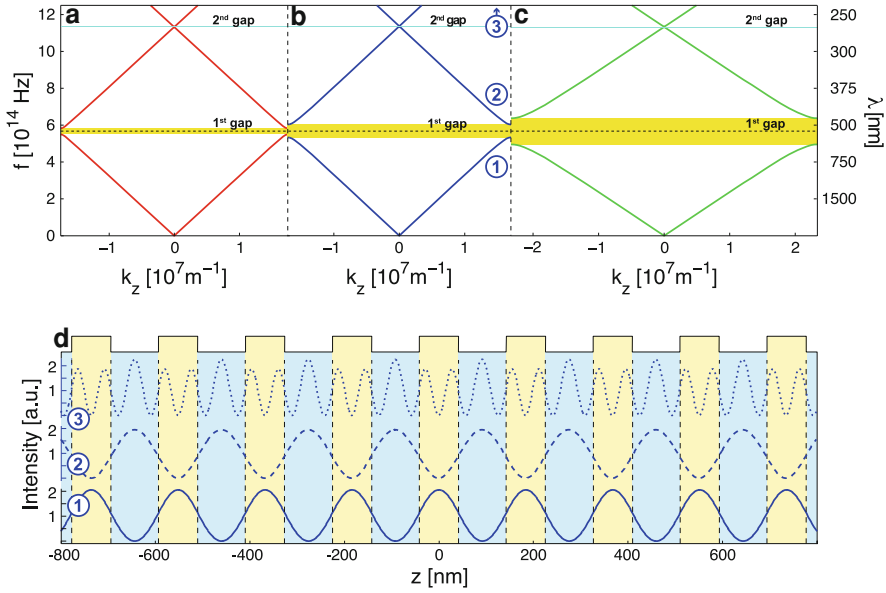


**Fig. 2.6** Band diagrams and field distributions of infinitely extended 1D photonic crystals. **a-c** The first Brillouin zone in the dispersion diagrams of three different multilayer structures for light propagation perpendicular to the layer planes. The corresponding refractive indices are shown in Table 2.2 together with the film thicknesses of the layers in each of the three infinite stacks, which were chosen in order to give a mid-gap wavelength of 530 nm (*dashed line*) for all three material combinations. The refractive index contrast,  $\hat{n} = \frac{n_1}{n_2}$  is increasing from left to right. **a**  $\hat{n} = 1.09$ , **b**  $\hat{n} = 1.21$ , **c**  $\hat{n} = 1.48$ . For each refractive index contrast, the first two bands are displayed. 1D photonic crystals always show band-gaps (shaded areas, yellow and blue in online version) for wave propagation along the direction of periodicity; the size of the gaps depends on  $\hat{n}$ . **d** Field distribution inside the infinite photonic crystal system with  $\hat{n} = 1.21$  for modes at the edges of the first three bands with their positions marked in the band diagram in (b)

a  $\frac{\lambda}{4}$ -multilayer stack (Fig. 2.7,  $m$  is a positive number). This arrangement allows the existence of localised states in the defect layer at frequencies  $f = \frac{mc}{2n_j d_j}$  within the band-gap of the quarter-wave stack. Here  $n_j$  and  $d_j$  are the refractive index and the thickness of the defect layer. Light with these frequencies can propagate through the structure, as it fulfils the resonance condition  $m\frac{\lambda}{2} = n_j d_j$ .

Bragg mirrors, made from titania and alumina layers with refractive indices  $n_{\text{TiO}_2} = 2.45$ ,  $n_{\text{Al}_2\text{O}_3} = 1.65$  and film thicknesses of  $d_{\text{TiO}_2} = 56$  nm,  $d_{\text{Al}_2\text{O}_3} = 83$  nm, have a peak reflectance wavelength of  $\lambda \approx 550$  nm (for more details on the materials see Chap. 3). The reflection characteristics of a free-standing Bragg filter consisting of a cavity layer of alumina with thickness  $d_{\text{cavity}}$  between two of the above described Bragg mirrors are displayed in Fig. 2.7 as a function of defect layer thickness and layer number of the Bragg mirrors enclosing the cavity layer. The bandwidth of a multilayer resonance cavity decreases as the number of layers in the Bragg stacks increases (Fig. 2.7d). This is expressed in the quality factor of a cavity

**Table 2.2** Multilayer material combinations used for band-gap calculations

|       | Constituent 1     |       |            | Constituent 2          |       |            |
|-------|-------------------|-------|------------|------------------------|-------|------------|
|       | Material          | $n_1$ | $d_1$ (nm) | Material               | $n_2$ | $d_2$ (nm) |
| ■ a ■ | PSPI              | 1.54  | 86         | Polydimethylsiloxane   | 1.41  | 94         |
| ■ b ■ | Polystyrene       | 1.59  | 83         | Teflon <sup>®</sup> AF | 1.31  | 101        |
| ■ c ■ | Titanium(II)oxide | 2.45  | 54         | Aluminium oxide        | 1.65  | 80         |

The colours (letters) in the first column correspond to the colours (subfigure labels) in Fig. 2.6. PSPI stands for polystyrene-polyisoprene triblock copolymer. Further information about the displayed materials can be found in Chap. 3

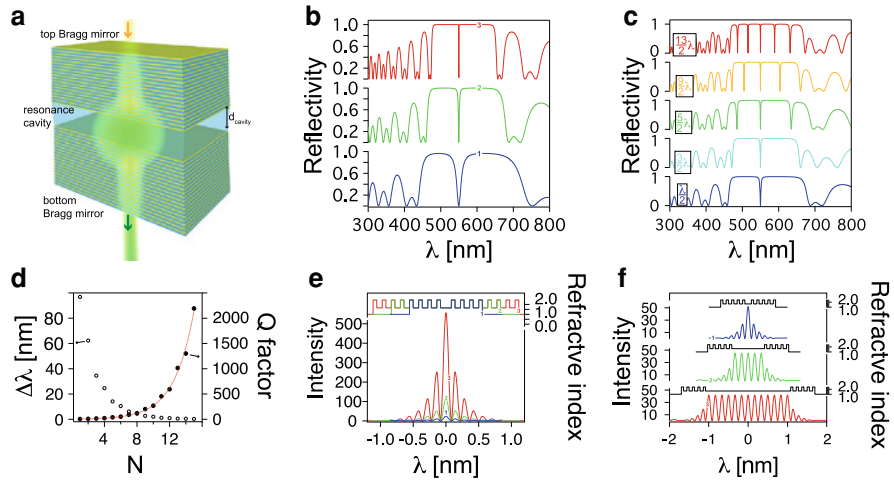


**Fig. 2.7** Multilayer interference filter. **a** Schematic drawing of a filter with two  $N$ -layered Bragg mirrors enclosing a resonance cavity of thickness  $d_{\text{cavity}}$ . **b** Reflectivity of a Bragg filter with a cavity layer thickness of  $d_{\text{cavity}} = \frac{\lambda}{2}$  for increasing layer numbers  $N$  in the two Bragg mirrors, five layers (curve “1”, blue in online version), nine layers (curve “2”, green in online version), 15 layers (curve “3”, red in online version). **c** Reflectivity of Bragg filters with different cavity thicknesses in multiples of  $\frac{\lambda}{2}$ . **d** Calculated bandwidth (white circles) and quality factor (black circles) of a  $\frac{\lambda}{2}$ -resonance cavity as a function of layer number in the top and bottom Bragg mirrors. **e** Field distributions inside  $\frac{\lambda}{2}$ -resonance cavities enclosed by Bragg mirrors of layer number  $N = 7$  (curve “1”, blue in online version),  $N = 11$  (curve “2”, green in online version),  $N = 15$  (curve “3”, red in online version). **f** Field distributions inside a Bragg filter for varying cavity layer thicknesses,  $d_{\text{cavity}} = \frac{\lambda}{2}$  (curve “1”, blue in online version),  $d_{\text{cavity}} = \frac{5\lambda}{2}$  (curve “2”, green in online version), and  $d_{\text{cavity}} = \frac{13\lambda}{2}$  (curve “3”, red in online version)



$Q = \frac{\lambda_{pb}}{\Delta\lambda}$  where  $\lambda_{pb}$  and  $\Delta\lambda$  are the centre wavelength and the width of the pass-band. The  $Q$ -factor is a measure for the losses of field intensity that a light wave incurs in a cavity per field oscillation period due to scattering or adsorption. The higher the  $Q$ -factor, the smaller are these losses and the higher are the maximum field strengths that can build up in the cavity for a wave that satisfies the resonance condition.

## 2.6 Diffraction from Periodic Surface Structures

Surfaces or materials with a lateral periodicity of the order of several wavelengths impose an amplitude and/or phase modulation on an incident light wave that can be detected in the transmitted and reflected wave part as a characteristic diffraction pattern. In the following, the discussion will concentrate on the reflection of light from a phase grating with high transparency and uniform material properties. The grating has a periodicity  $p$  in the  $x$ -direction. It is uniform in the  $y$ -direction and its surface normal is oriented parallel to the  $z$ -direction (Fig. 2.8). Consider a spherical light wave with intensity  $I_0(x_0, z_0)$  originating from the point  $(x_0, z_0)$  travelling in the  $x$ - $z$ -plane towards the grating situated in the “ $z = 0$ ”-plane (Fig. 2.8, the  $y$ -dimension is not relevant for this discussion). A diffraction pattern, caused by the interaction of that wave with the grating is observed on a cylindrical screen with radius  $L$  centered at the grating position and intensities  $I(x, z)$  are detected at points  $(x, z)$  on the screen.

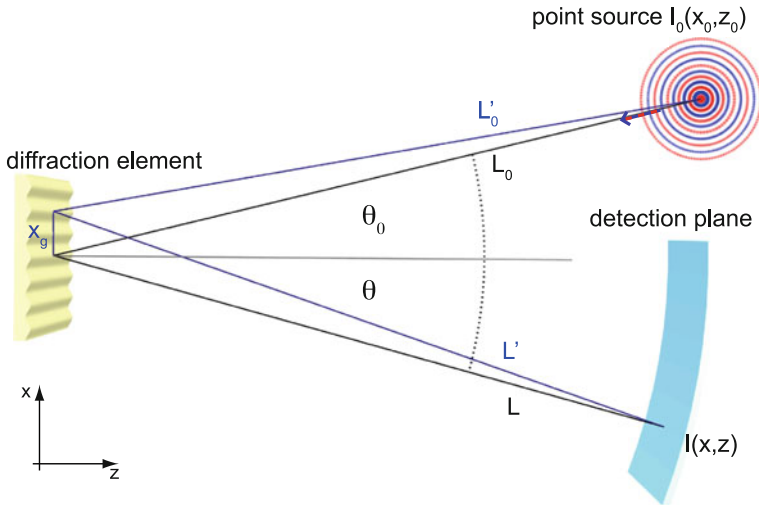


**Fig. 2.8** Geometry of the diffraction problem. Light from a point source at a distance  $L_0$  is scattered from the grating and the diffraction pattern is detected on a screen at a distance  $L$  from the grating

### 2.6.1 Diffraction in the Fraunhofer Approximation

If the distance  $L_0$  of the light source to the diffracting object is large enough compared to the light wavelength  $\lambda$ , the waves incident on the grating can be treated as plane waves. If in addition the distance  $L$  of the observation point to the grating is large compared to the grating periodicity and the light wavelength, the observation point is said to be lying in the far-field and the diffraction problem can be treated in the Fraunhofer approximation [2].

The reflection function  $F_g$  of one periodic grating element is defined by

$$F_g(x_g) = \frac{V(x_g)}{V_0(x_g)}$$

where the disturbance  $V(x_g)$  of the light wave caused by the grating element is weighted by the default disturbance  $V_0(x_g) = e^{ik \sin \theta_0 x_g}$  when no grating is present. For a phase grating, consisting of a transparent dielectric, that is observed in reflection,  $F_g(x_g)$  satisfies  $|F_g| = r$ , where  $r$  is the Fresnel reflection coefficient of the dielectric material. The function  $F_g(x_g)$  depends on the particular form of the grating unit cell.

The Fraunhofer approximation of the Kirchhoff–Fresnel diffraction integral, which describes the field amplitude observed at point  $(x, z)$  on the screen, after light has been diffracted from one periodic grating element, is given by

$$S(x_0, z_0, x_1, z_1) = -\frac{i(\cos \theta + \cos \theta_0)}{2\lambda L_0 L} \int_{-\frac{g}{2}}^{\frac{g}{2}} F_g(x_g) e^{ik(L'(x, z, x_g) + L'_0(x_0, z_0, x_g))} dx_g \quad (2.26)$$

where the approximation

$$\begin{aligned} L_0'^2 &= (x_0 - x_g)^2 + z_0^2 \approx L_0 - \frac{x_0}{L_0} x_g \\ L'^2 &= (x - x_g)^2 + z^2 \approx L - \frac{x}{L} x_g \end{aligned}$$

together with

$$\begin{aligned} \frac{x_0}{L_0} &= -\sin \theta_0 \\ \frac{x}{L} &= \sin \theta \end{aligned}$$

leads to the reflection function of one periodic element of the grating

$$S(\theta, \theta_0) = -\frac{i(\cos \theta + \cos \theta_0)}{2\lambda L_0 L} e^{ik(L_0 + L)} \int_{-\frac{g}{2}}^{\frac{g}{2}} F_g(x_g) e^{-ik(\sin \theta - \sin \theta_0)x_g} dx_g. \quad (2.27)$$

The field distribution  $U$  at point  $(x, z)$ , otherwise defined by its distance  $L$  from the grating centre and the angle  $\theta$  to the surface normal of the grating, follows from summation over all the contributions of the  $N$  individual grating unit cells as

$$\begin{aligned} U(\theta, \theta_0) &= S(\theta, \theta_0) \cdot \sum_{n=0}^{N-1} e^{-inpk(\sin \theta - \sin \theta_0)} \\ &= S(\theta, \theta_0) \cdot \frac{1 - e^{-iNpk(\sin \theta - \sin \theta_0)}}{1 - e^{-ipk(\sin \theta - \sin \theta_0)}} \end{aligned} \quad (2.28)$$

The field, observed at an angle  $\theta$ , is essentially a superposition of plane waves resulting from the unit cells of the grating, each of them modulated in the same way by the reflection function of a grating unit cell.

The intensity observed in distance  $L$  at an angle  $\theta$  is then given by

$$I(\theta, \theta_0) = |U(\theta, \theta_0)|^2 = |S(\theta, \theta_0)|^2 \cdot \left( \frac{\sin \frac{Npk(\sin \theta - \sin \theta_0)}{2}}{\sin \frac{pk(\sin \theta - \sin \theta_0)}{2}} \right)^2. \quad (2.29)$$

The results of this approximation for large angles of light incidence  $\theta_0$  and detection  $\theta$  have to be considered with caution as the implied simplifications might not necessarily apply. By suitable normalisation  $\frac{S(\theta, \theta_0)}{S_0(\theta, \theta_0)}$ , where  $S_0(\theta, \theta_0)$  is the reflection function of a 100%-reflective, phase-conserving plane mirror, the pre-factor of the integral giving the reflection function  $S(\theta, \theta_0)$  of one periodic element vanishes.

This approximation was employed to model the diffraction from a simple square phase grating. The results were compared to MEEP Finite-Difference Time-Domain simulations of the same square grating to test the reliability of the MEEP algorithm, before applying it to model diffraction from structures with more complex unit cell profiles. The results of this comparison are presented in Fig. 2.10, after a short introduction in the FDTD simulations of diffraction with MEEP.

### 2.6.2 Finite-Difference Time-Domain Modelling of Diffraction

MEEP, a FDTD simulation package, is widely used for computational electromagnetism [7]. MEEP has been programmed by D. Roundy, M. Ibanescu, P. Bermel and S. G. Johnson at the Massachusetts Institute of Technology.

MEEP solves Maxwell's field equations in a particular dielectric structure and its vicinity, by discretising time and space on a finite rectangular grid with a spatial resolution  $\Delta x$  and a temporal resolution  $\Delta t < \frac{n_{\min}}{\sqrt{N_D}} \Delta x$  [7]. Here,  $n_{\min}$  is the minimum refractive index ( $n_{\min} = 1$  for air) and  $N_D$  is the number of relevant system dimensions. For the discretisation of the field equations with second-order accuracy, MEEP uses Yee lattices, storing different field components for different grid locations [11]. If all field components at a specific point on the lattice need to be

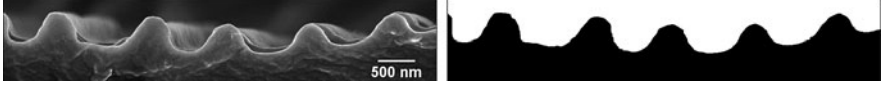


**Fig. 2.9** A grating structure, and its binary image for MEEP. Electron micrograph and a binarised image of the grating structure found on the surface of wild tulips. SEM image taken from the surface of *Tulipa kolpakowskiana*

known, they can be obtained by interpolation. In general this approach is not problematic but it can cause some inaccuracies if fields are read out very close to dielectric boundaries, across which they might be discontinuous.

The MEEP package can be controlled via C++ libraries or a scheme script, tailored to the specific application. For calculations of diffraction, a C++ interface has been implemented in the context of this thesis. The C++ algorithm can acquire refractive index maps from image files. These image files might be refractive index maps that have been created, based on contrasts in SEM or TEM pictures (for instance shown in Fig. 2.9).

Diffraction from periodic micro-structures can be simulated in two dimensions by looking at diffraction from a unit cell, while implementing periodic boundary conditions on the sides of the simulation volume to account for the periodicity of such a grating (Fig. 2.10a). The top and the bottom of the simulation volume are delimited by “perfectly matched layers” (PML). These boundary layers absorb any incident waves, preventing artefacts that could result from spurious interferences with re-entrant waves. Detectors are positioned at sufficient distances from the diffracting interface to avoid coupling with evanescent surface modes. A plane-wave Gaussian pulse is created at an appropriate distance from the grating interface (Fig. 2.10b). Depending on its width, the pulse contains a range of frequencies. This pulse is propagated through the structure in discrete time steps  $\Delta t$  by solving Maxwell’s equations at each point of the Yee lattice to acquire the relevant field values at this point. The reflected and transmitted fields (Fig. 2.10c) are detected at the coordinates  $y_r$  and  $y_t$  in the unit cell for each time step  $n$  giving  $E_r(x, y_r, n \cdot \Delta t)$  and  $E_t(x, y_t, n \cdot \Delta t)$ , shown in Fig. 2.10d. Fourier transformation in time

$$E_{r,t}(x, f) = \int_0^{t_{\max}} E_{r,t}(x, t) \cdot e^{-i2\pi ft} dt \quad (2.30)$$

gives the electric fields as a function of position and frequency. Fourier transformation along the space coordinate  $x$

$$E_{r,t}(k_x, f) = \int_{-\frac{g}{2}}^{\frac{g}{2}} E_{r,t}(x, \omega) \cdot e^{-ik_x x} dx \quad (2.31)$$

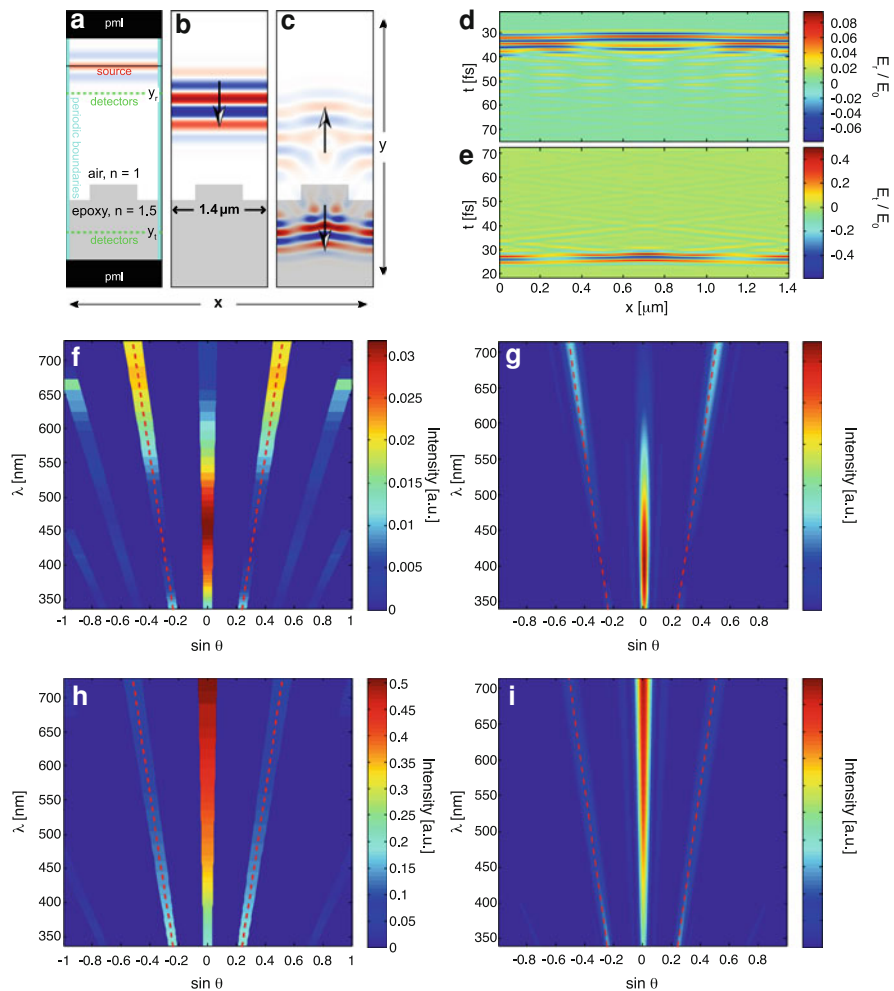


**Fig. 2.10** Diffraction grating simulation with MEEP. **a** Representation of the computational volume displaying the refractive index map of a square phase grating unit cell, “perfectly matching layers”, source and detector positions. **b** Gaussian pulse of light with wavelengths ranging from 300 to 800 nm propagating towards the grating interface. **c** Reflected and transmitted parts of the incident wave packet. **d, e** Field amplitudes measured in the planes of the reflection (**d**) and transmission (**e**) detector as a function of time and  $x$ -coordinate on the detector. There is good agreement between the diffraction patterns, observed in reflection for the FDTD simulations (**f**) and for calculations in the Fraunhofer approximation (**g**). **h** and **i** show the diffraction patterns observed in transmission for the simulations and the scattering calculations in the Fraunhofer approximation. The *dashed lines* in (**f**–**i**) represent the first and  $-$ first diffraction orders as a function of  $\lambda$  and sine of  $\theta$  determined by the grating equation  $\lambda = \pm p \sin \theta$

allows the determination of the electric fields as a function of wave vector and frequency. The integration boundaries for the second transformation are given by the unit cell width  $p$ .

Using the relations

$$\begin{aligned}\lambda &= \frac{c}{f}, \\ \sin \theta &= \frac{k_x}{k} = \frac{k_x c}{2\pi f}, \\ I_{r,t} &= E_{r,t}^* \cdot E_{r,t}\end{aligned}$$

the intensity  $I(\lambda, \theta)$  of light can be plotted as a function of the diffraction angle  $\theta$ , which is measured from the sample normal. Note that the incidence angle is  $\theta_0 = 0$  for the results in Fig. 2.10, which shows simulations of diffraction from a square-profile phase grating with  $p = 1.4 \mu\text{m}$ . The simulated reflected and transmitted intensities  $I_r^{\text{sim}}(\lambda, \theta)$  and  $I_t^{\text{sim}}(\lambda, \theta)$  are plotted in Fig. 2.10f, h. For comparison, the reflected and transmitted intensities  $I_r^{\text{calc}}(\lambda, \theta)$  and  $I_t^{\text{calc}}(\lambda, \theta)$ , which have been obtained by evaluation of the Fresnel–Kirchhoff diffraction formula in the Fraunhofer approximation (as described above), are displayed in Fig. 2.10g, i. For the simple case of a square-profile phase grating, there is a good agreement between the data obtained in simulations and in approximative calculations for the intensities detected in the far field. FDTD simulations with MEEP could potentially be used to model diffraction from more complicated periodic geometries found in the form of regular striations on the petals of wild tulip species (Sect. 2.2).

These calculations were performed with the help of Moritz Kreysing, who pioneered the use of MEEP in the Biological and Soft Systems sector and the Nanophotonics group of the Cavendish Laboratory and played a leading role in realising the diffraction simulations.

## References

1. Land, M.: The physics and biology of animal reflectors. *Prog. Biophys. Mol. Biol.* **24**, 75 (1972)
2. Born, M., Wolf, E.: *Principles of Optics*. Cambridge University Press, Cambridge (2005)
3. Allen Taflove, S.C.H.: *Computational Electrodynamics: The Finite-Difference Time-Domain Method*. Artech House, Dedham (1995)
4. Joannopoulos, J.D., Johnson, S.G., Winn, J.N., Meade, R.D.: *Photonic Crystals: Molding the Flow of Light*. Princeton University Press, Princeton (2008)
5. Heavens, O.: *Optical Properties of Thin Solid Films*. Dover Publications, New York (1965)
6. Johnson, S.G., Joannopoulos, J.D.: Block-iterative frequency-domain methods for Maxwell's equations in a planewave basis. *Opt. Express* **8**, 173–190 (2001)
7. Oskooi, A.F. et al.: MEEP: a flexible free-software package for electromagnetic simulations by the FDTD method. *Comp. Phys. Comm.* **181**, 687–702 (2010)
8. Kinoshita, S., Yoshioka, S.: Structural colors in nature: The role of regularity and irregularity in the structure. *ChemPhysChem* **6**, 1442–1459 (2005)

9. Mahlein, H.: Generalized Brewster-angle conditions for quarter-wave multilayers at non-normal incidence. *J. Opt. Soc. Am* **64**, 647–653 (1974)
10. Kittel, C.: *Introduction to Solid State Physics*. Wiley, New York (1996)
11. Yee, K.S.: Numerical solution of initial boundary value problems involving maxwell's equations in isotropic media. *IEEE T. Antenn. Propag.* **14**, 302–307 (1966)



<http://www.springer.com/978-3-642-15168-2>

Photonic Structures Inspired by Nature

Kolle, M.

2011, XVI, 144 p., Hardcover

ISBN: 978-3-642-15168-2